JOURNAL OF AIRCRAFT
Vol. 45, No. 4, July–August 2008

Measurement-Integrated Simulation of Clear Air Turbulence Using a Four-Dimensional Variational Method

Takashi Misaka* and Shigeru Obayashi†
Tohoku University, Sendai 980-8577, Japan
and
Eiichi Endo‡
Japan Aerospace Exploration Agency, Mitaka, Tokyo 181-0015, Japan

DOI: 10.2514/1.34111

An unsteady flow phenomenon of clear air turbulence was investigated by numerical simulation integrating flight data of encounters with severe turbulence. To determine the initial condition of the numerical simulation based on the flight data, the four-dimensional variational method was employed. The validation of the present method was conducted by using pseudo flight data that are obtained from a reference flowfield produced by the numerical simulation. Then the four-dimensional variational method was applied to two actual severe turbulence cases to reproduce the flowfield of these turbulent flows. The validation results show reproducibility of the flowfield, even with spatially limited measurement data such as flight data, as long as the data involve primary flow features. Unsteady flowfields of turbulence were successfully simulated by using the four-dimensional variational method based on two cases of actual flight data. The results show the existence of vortices that correspond to clear air turbulence. In addition, the existing hazard indices *F*-factor and root-mean-square normal load were applied to the reproduced flowfield to obtain a spatial distribution of these hazard indices.

Nomenclature

C_p	=	heat ratio for constant pressure
$\boldsymbol{E}$, $\boldsymbol{F}$	=	viscous and inviscid fluxes in the x and y directions
e	=	total energy per unit volume
F	=	F-factor
g	=	gravity acceleration, m/s^2
H	=	enthalpy
H_i	=	measurement operator
H_i^A	=	adjoint operator of H_i, transpose of H_i^L
H_i^L	=	linearized operator of H_i
J	=	objective function
L	=	Lagrangian
L_x	=	integration interval for σ_w
M_i	=	Navier–Stokes equations written as a time-advancing operator
M_i^A	=	adjoint operator of Navier–Stokes equations, transpose of M_i^L
M_i^L	=	linearized operator of M_i
N	=	number of time steps for numerical simulation
N_f	=	number of data along the flight path
p	=	pressure, Pa
p_0	=	reference pressure, 10^5, Pa
$\boldsymbol{Q}$, $\boldsymbol{Q}_i$	=	primitive flow variables
q_x, q_y	=	heat fluxes in the x and y directions
R	=	gas constant for air, 287, J/(kg · K)
R_i	=	measurement error covariance matrix
R'	=	modified gas constant, $R^\gamma p_0^{1-\gamma}$
$\boldsymbol{S}$	=	gravity term
T	=	temperature, K
t	=	time, s
$\boldsymbol{U}$	=	conservative flow variables
u, v	=	velocity in the x and y directions, m/s
V_a	=	air speed
V_g	=	ground speed
$\bar{v}$	=	average of the vertical wind in the interval of L_x
x, y	=	horizontal (flight path) and vertical (altitude) coordinates, m
$\boldsymbol{y}_i$	=	measurement vector
Γ	=	transformation matrix of flow variables
γ	=	specific heat ratio, 1.4
Δn	=	normal load, g
θ	=	potential temperature, K
$\boldsymbol{\lambda}_i$	=	adjoint variables, Lagrangian multiplier
π	=	Exner function
ρ	=	density, kg/m^3
$\sigma_{\Delta n}$	=	root-mean-square normal load
σ_w	=	root-mean-square vertical wind
τ_{xx}, τ_{xy}, τ_{yy}	=	viscous tensor

Subscripts

i	=	index for the time step
j, k	=	indices for the x and y directions

I. Introduction

CLEAR air turbulence (CAT) has a serious impact on aviation safety, and in some cases, it results in serious injury of crew and passengers. CAT is not detected by existing airborne radar because CAT is not associated with rain clouds, which reflect radio waves. Kelvin–Helmholtz (K–H) instability is known as one of the causes of CAT; however, the detailed mechanisms of CAT are not yet fully understood. The reasons are considered to be the difficulty in finding its existence and the lack of observed data. Although the measurement of temperature inversion will help to locate the shear layer and a regional weather prediction will tell us of a hazardous region of turbulence, their spatial resolution is not enough for avoidance of CAT. For these reasons, a turbulence-prediction method based on forward-looking in situ velocity measurements is strongly desired for aviation safety.

Presented as Paper 81 at the 45th AIAA Aerospace Science Meeting and Exhibit, Reno, NV, 8–11 January 2007; received 18 August 2007; revision received 9 October 2007; accepted for publication 28 October 2007.

*Graduate Student, Institute of Fluid Science. Student Member AIAA.
†Professor, Institute of Fluid Science. Associate Fellow AIAA.
‡Associate Senior Researcher.

The Japan Aerospace Exploration Agency (JAXA) has been developing an airborne turbulence-detection system using light detection and ranging (lidar) [1,2]. Flight tests were successfully conducted using the resulting 2-km-range lidar. A lidar of 10-km range is under development to obtain enough measurement range. The objective of the lidar is to perform forward-looking measurements of airflow velocity for the detection of CAT. A lidar measures the local velocity of the atmosphere by detecting a Doppler shift in light scattered by aerosols such as dust and vapor in the atmosphere; therefore, the measurement data obtained from the lidar are the velocity components in the forward direction. For this reason, an algorithm that detects the existence of turbulence from lidar measurements is required for the practical application of the lidar. As candidates of such algorithms, several algorithms that compute hazard indices have been proposed, not only for CAT, but also for wind shear [3–6]. A wind-shear-prediction algorithm to be coupled with radar or lidar measurements was proposed by Stratton and Stengel [7]. In their research, a parameterized microburst model was used to optimize the parameters in the prediction model. A more realistic representation of a turbulence flowfield would improve the turbulence-detection capability of these wind-shear-prediction algorithms.

Regarding the research related to the flowfield of air turbulence, a model that represents a flowfield by a combination of two-dimensional vortices was used to identify CAT based on flight data [8,9]. Numerical simulations of air turbulence have also been performed based on large eddy simulation (LES) in [10–16]. They investigated several kinds of air turbulence, such as convectively induced turbulence and wake turbulence. In that research, a finer computational mesh was employed than that for a regional weather prediction. As described by Hamilton and Proctor [10], a mesh resolution of 50 m is needed to capture at least 97% of the cumulative aircraft load distribution. They also mentioned a certification toolset for a newly developed airborne turbulence-detection system based on a numerical simulation of air turbulence [11]. LES of air turbulence would allow a more realistic flowfield characterization in comparison with the simple vortex model; however, the setting of initial and boundary conditions of air turbulence is not a trivial problem, due to its unsteadiness and a computational domain with open boundaries.

Use of observation data to improve the reliability of numerical simulation is known as data assimilation in the community of numerical weather simulation scientists. Data assimilation techniques such as the four-dimensional variational (4D-var) method [17] and ensemble Kalman filter (EnKF) [18] determine a flowfield based on observation data; therefore, they can reduce the dependency of simulated flowfield on an artificial setting of initial and boundary conditions. In the case of the 4D-var method, the initial flowfield is set in such a way that the unsteady flow computation starting from this initial condition will result in a flowfield that matches the corresponding measurements in time. On the other hand, the EnKF sequentially modifies a numerical solution based on the difference between numerical and measurement result when considering model and measurement errors. Funamoto et al. [19] proposed an integration method of numerical flow simulation and ultrasonic measurements for medical application, the named ultrasonic-measurement-integrated (UMI) simulation method. The UMI simulation method was applied to the flow in an aorta in which ultrasonic color Doppler measurements are used to compensate inaccuracy of numerical flow simulation. In the present research using flight data that are composed of spatially limited time-series measurements, the 4D-var method produces a flowfield that is more kinematically consistent with the flight data. It is because the 4D-var method recalculates the flowfield to find an initial condition, such that the simulated result best fits the measurements within the assimilation-time interval. This means that any forcing term due to the difference between numerical and measurement results is not applied during the numerical simulation of the flowfield. On the other hand, a flowfield is modified sequentially based on measurement data during a single run of numerical simulation of the flowfield in the case of sequential data assimilation techniques such as EnKF [20].

As a step to construct a CAT-detection algorithm based on a detailed representation of the flowfield, the present research attempts to reproduce the flowfield of CAT by integrating numerical simulation of atmospheric flow and the flight data acquired during encounters with CAT. In the numerical simulation, the gravity term was considered, and the 4D-var method was applied to incorporate flight data into the numerical simulation. This paper describes the formulation and numerical method of the 4D-var method for the integration of the flight data at first. Because measurement data in this research are spatially limited to those on the flight path, the validation of the capability to reproduce a flowfield by the limited measurements is conducted using several idealized test cases. Then the results based on actual flight data are presented. In addition, distributions of the hazard indices F-factor and root-mean-square normal load, which were obtained from the reproduced flowfield, are shown. These hazard indices evaluated from the reproduced flowfield could be used as a reference hazard field for the evaluation of the hazard indices obtained from radar or lidar simulation, as described by Hamilton and Proctor [11].

II. Methods

A. Basic Equations and Numerical Method

Basic equations are the two-dimensional compressible Navier–Stokes equations:

$$\frac{\partial \boldsymbol{U}}{\partial t} + \frac{\partial \boldsymbol{E}}{\partial x} + \frac{\partial \boldsymbol{F}}{\partial y} = \boldsymbol{S} \tag{1}$$

Conservative variables $\boldsymbol{U} = [\rho, \rho u, \rho v, e]^t$ are converted into primitive variables of $\boldsymbol{Q} = [p, u, v, \theta]^t$, which are used in the field of weather prediction:

$$\frac{\partial \boldsymbol{Q}}{\partial t} + \Gamma^{-1}\left(\frac{\partial \boldsymbol{E}}{\partial x} + \frac{\partial \boldsymbol{F}}{\partial y} - \boldsymbol{S}\right) = 0 \tag{2}$$

where $\boldsymbol{Q}$, $\boldsymbol{E}$, $\boldsymbol{F}$, and $\boldsymbol{S}$ are expressed as follows:

$$\boldsymbol{Q} = \begin{bmatrix} p \\ u \\ v \\ \theta \end{bmatrix}, \qquad \boldsymbol{E} = \begin{bmatrix} \rho u \\ \rho u^2 + p - \tau_{xx} \\ \rho uv - \tau_{xy} \\ (e+p)u - (\tau_{xx}u + \tau_{xy}v + q_x) \end{bmatrix} \tag{3}$$

$$\boldsymbol{F} = \begin{bmatrix} \rho v \\ \rho uv - \tau_{xy} \\ \rho v^2 + p - \tau_{yy} \\ (e+p)v - (\tau_{xy}u + \tau_{yy}v + q_y) \end{bmatrix}, \qquad \boldsymbol{S} = \begin{bmatrix} 0 \\ 0 \\ \rho g \\ \rho v g \end{bmatrix} \tag{4}$$

$$\Gamma = \frac{\partial \boldsymbol{U}}{\partial \boldsymbol{Q}} = \begin{bmatrix} \rho_p & 0 & 0 & \rho_\theta \\ \rho_p u & \rho & 0 & \rho_\theta u \\ \rho_p v & 0 & \rho & \rho_\theta v \\ \rho_p H - 1 & \rho u & \rho v & \rho_\theta H + \rho C_p \end{bmatrix} \tag{5}$$

Inviscid and viscous fluxes in the second term in the left side of Eq. (1) are converted by multiplying the inverse of transformation matrix in Eq. (5), in which subscripts p and θ represent derivatives in terms of p and θ, respectively. The equation of state for ideal gas, $p = \rho RT$, was employed to close the Navier–Stokes equations. The equation of state is rewritten by using the potential temperature, instead of the temperature based on a relation between the potential temperature and temperature, $\theta = T(p/p_0)^{(\frac{1}{\gamma}-1)}$, as follows:

$$p = R'(\rho\theta)^\gamma, \qquad R' = R^\gamma p_0^{1-\gamma} \tag{6}$$

where p_0 denotes a reference pressure and is set to 10^5, Pa.

Inviscid numerical flux is computed based on Roe's flux-difference splitting method using primitive variables interpolated by a monotonic upwind scheme for conservation laws (MUSCL) scheme [21]. A total-variation-diminishing limiter is not used in the

MUSCL interpolation. The viscous term is evaluated by the second-order central-difference scheme. Numerical simulation is performed based on the standard Smagorinsky model with $C_s = 0.16$, in which rotation correction was not applied [16]. The fourth-order Runge-Kutta method is used for the time integration.

B. Boundary and Initial Conditions

A sponge boundary condition, which gradually decreases the update rate of the solution near the boundary, is used for the upper and lower boundaries. The mesh spacing near these boundaries is increased to form a buffer region. A free boundary condition based on characteristic velocity is applied to the left and right boundaries.

Vertical profiles of the horizontal velocity and potential temperature are given as initial conditions of the 4D-var method. These variables are set to constant for the horizontal direction. The initial condition of vertical velocity is set to zero. The initial condition of pressure is given by the following equations to obtain hydrostatic equilibrium under the normal gravity condition:

$$p = p_0 \pi^{\frac{c_p}{R}}, \qquad \pi = \pi_g - \frac{g}{C_p}\int_0^y \frac{1}{\theta}\,\mathrm{d}y \tag{7}$$

where π_g is an Exner function at the ground surface.

C. Measurement-Integration Method

The 4D-var method is employed to integrate the flight data into the numerical simulation. The objective of data assimilation based on the 4D-var method is to obtain an initial flow condition that reproduces corresponding measurements during the unsteady flow simulation, starting from this initial flow condition [17]. Figure 1 shows a schematic of the 4D-var method. Vertical and horizontal axes show flow state and time, respectively. A solid line shows a trajectory of the real flow state. Broken lines show trajectories of the simulated flow state, starting from different initial conditions. The 4D-var method is the method to obtain the initial condition of the real flow state by evaluating the difference in these trajectories.

The differences of measurements (usually, measurements have less information than with the numerical simulation) and corresponding numerical results evaluated by conducting the numerical simulation over a period of time are represented as an objective function with respect to an initial flow variable $\boldsymbol{Q}_0$:

$$J(\boldsymbol{Q}_0) = \frac{1}{2}\sum_{i=0}^{N}[H_i(\boldsymbol{Q}_i) - \boldsymbol{y}_i]^T R_i^{-1}[H_i(\boldsymbol{Q}_i) - \boldsymbol{y}_i] \tag{8}$$

where H_i is an observation operator that converts the dimension of computational flow variables into that of measurement data to evaluate these differences. Subscript i shows a time step of the flow computation, and N is the total time number of time steps. Equation (8) is a function of $\boldsymbol{Q}_0$; that is, the measurement-integration process is formulated as a minimization problem of $J(\boldsymbol{Q}_0)$ with a control variable of $\boldsymbol{Q}_0$. The 4D-var method has the capability to treat measurement error through a measurement error covariance matrix R_i; its elements are the covariances between each measurement points. It is a reasonable assumption that measurement errors made at different location are uncorrelated [20]. In that case, R_i becomes a diagonal matrix, which consists of variances of measurement error at each measurement location. In addition to this assumption, the variances of measurement error at each measurement location were set to unity: that is, R_i is a unit matrix The estimation of the velocity vector from flight data involves an error due to an interpolation of the time series data; therefore, the appropriate estimation of measurement error variances of the reproduced velocity vector is not straightforward, and it exceeds the scope of this paper.

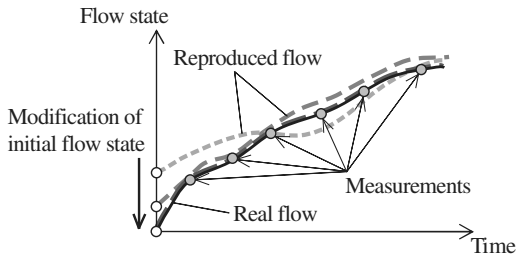

Fig. 1 Schematic of measurements integration procedure based on 4D-var method.

To obtain the gradient of $J(\boldsymbol{Q}_0)$ used for the minimization of $J(\boldsymbol{Q}_0)$, a Lagrange function is introduced using a Lagrange multiplier vector $\boldsymbol{\lambda}_i$, as follows:

$$\begin{aligned} L &= J(\boldsymbol{Q}_0) + \sum_{i=1}^{N}[M_{i-1}(\boldsymbol{Q}_{i-1}) - \boldsymbol{Q}_i]^T\boldsymbol{\lambda}_i \\ &= \frac{1}{2}\sum_{i=0}^{N}[H_i(\boldsymbol{Q}_i) - \boldsymbol{y}_i]^T R_i^{-1}[H_i(\boldsymbol{Q}_i) - \boldsymbol{y}_i] \\ &\quad + \sum_{i=1}^{N}[M_{i-1}(\boldsymbol{Q}_{i-1}) - \boldsymbol{Q}_i]^T\boldsymbol{\lambda}_i \end{aligned} \tag{9}$$

where M_i represents the Navier–Stokes equation operator written as a time-evolution operator, which is a nonlinear function of $\boldsymbol{Q}_i$. The gradient of $J(\boldsymbol{Q}_0)$ is obtained through the process to find a saddle point of the Lagrange function (9): that is, a point at which the partial derivatives of the Lagrange function (9) vanish simultaneously in the space spanned by $\boldsymbol{Q}_0$, $\boldsymbol{Q}_i$ and $\boldsymbol{\lambda}_i$ $(i = 1 \sim N)$. At a saddle point, $\partial L/\partial \boldsymbol{Q}_0 = 0$, $\partial L/\partial \boldsymbol{Q}_i = 0$, and $\partial L/\partial \boldsymbol{\lambda}_i = 0$ $(i = 1 \sim N)$. The requirements for $\partial L/\partial \boldsymbol{\lambda}_i = 0$ $(i = 1 \sim N)$ are satisfied by using the Navier–Stokes equation operator to advance $\boldsymbol{Q}_i$. The condition of the partial derivatives in terms of $\boldsymbol{Q}_N$,

$$\frac{\partial L}{\partial \boldsymbol{Q}_N} = -\boldsymbol{\lambda}_N + H_N^A R_N^{-1}[H_N(\boldsymbol{Q}_N) - \boldsymbol{y}_N] = 0 \tag{10}$$

gives

$$\boldsymbol{\lambda}_N = H_N^A R_N^{-1}[H_N(\boldsymbol{Q}_N) - \boldsymbol{y}_N] \tag{11}$$

where H_N^A is a transpose of a linearized measurement operator H_N^L. The condition of the partial derivatives in terms of $\boldsymbol{Q}_i$ $(i = 1 \sim N-1)$,

$$\begin{aligned} &\frac{\partial L}{\partial \boldsymbol{Q}_i} = -\boldsymbol{\lambda}_i + M_i^A\boldsymbol{\lambda}_{i+1} + H_i^A R_i^{-1}[H_i(\boldsymbol{Q}_i) - \boldsymbol{y}_i] = 0 \\ &\qquad (i = 1 \sim N-1) \end{aligned} \tag{12}$$

gives

$$\boldsymbol{\lambda}_i = M_i^A\boldsymbol{\lambda}_{i+1} + H_i^A R_i^{-1}[H_i(\boldsymbol{Q}_i) - \boldsymbol{y}_i], \qquad (i = 1 \sim N-1) \tag{13}$$

where M_i^A represents an adjoint operator of the Navier–Stokes equation, a transpose of a linearized Navier–Stokes equation operator M_i^L. The equation from the condition that the partial derivatives of the Lagrange function (9) with respect to $\boldsymbol{Q}_0$ gives the following equation:

$$\frac{\partial L}{\partial \boldsymbol{Q}_0} = M_0^A\boldsymbol{\lambda}_1 + H_0^A R_0^{-1}[H_0(\boldsymbol{Q}_0) - \boldsymbol{y}_0] \tag{14}$$

Because $L = L(\boldsymbol{Q}_0, \boldsymbol{Q}_i, \boldsymbol{\lambda}_i)$ and $\boldsymbol{Q}_i$ and $\boldsymbol{\lambda}_i (i = 1 \sim N)$ depend on $\boldsymbol{Q}_0$, the gradient of the Lagrange function L with respect to $\boldsymbol{Q}_0$ is obtained by the chain rule as follows:

$$\nabla_{\boldsymbol{Q}_0} L = \frac{\partial L}{\partial \boldsymbol{Q}_0} + \sum_{i=1}^{N}\left(\frac{\partial L}{\partial \boldsymbol{Q}_i}\frac{\partial \boldsymbol{Q}_i}{\partial \boldsymbol{Q}_0} + \frac{\partial L}{\partial \boldsymbol{\lambda}_i}\frac{\partial \boldsymbol{\lambda}_i}{\partial \boldsymbol{Q}_0}\right) \tag{15}$$

At a saddle point, $\partial L/\partial \boldsymbol{Q}_i = \partial L/\partial \boldsymbol{\lambda}_i = 0$ $(i = 1 \sim N)$. And $L = J$ when the Navier–Stokes equation is satisfied; that is, $\nabla_{\boldsymbol{Q}_0} L = \nabla_{\boldsymbol{Q}_0} J$. Therefore, the gradient of $J(\boldsymbol{Q}_0)$ is obtained as follows:

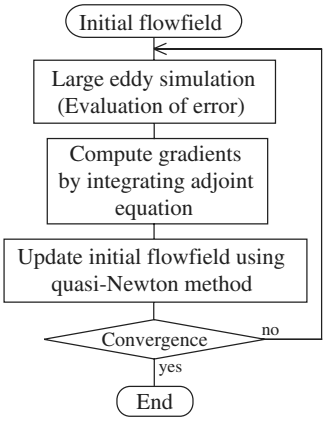

Fig. 2 Flowchart of the 4D-var method in the present study.

$$\nabla_{Q_0} J = \nabla_{Q_0} L = \frac{\partial L}{\partial \boldsymbol{Q}_0} = M_0^A \boldsymbol{\lambda}_1 + H_0^A R_0^{-1}[H_0(\boldsymbol{Q}_0) - \boldsymbol{y}_0] \tag{16}$$

The procedure to obtain the gradient is rewritten based on Eqs. (11), (13), and (16) as follows:

$$\boldsymbol{\lambda}_{N+1} = 0 \tag{17}$$

$$\boldsymbol{\lambda}_i = M_i^A \boldsymbol{\lambda}_{i+1} + H_i^A R_i^{-1}[H_i(\boldsymbol{Q}_i) - \boldsymbol{y}_i], \qquad (i = N, N-1, \ldots, 0) \tag{18}$$

$$\nabla J_{Q_0} = \boldsymbol{\lambda}_0 \tag{19}$$

Equations (17–19) show that the gradient of $J(\boldsymbol{Q}_0)$ is obtained by the inverse time integration of $\boldsymbol{\lambda}_i$ using the adjoint operator M_i^A with a force term: $H_i^A R_i^{-1}[H_i(\boldsymbol{Q}_i) - \boldsymbol{y}_i]$.

Figure 2 shows a flow chart of the 4D-var method. First, the initial flow condition is given by vertical profiles of the horizontal velocity and potential temperature. Pressure is set to hydrostatic equilibrium and vertical velocity is set to zero. Numerical simulation is performed through a certain period, with evaluation of the objective function equation (8). An adjoint forcing term in Eq. (18) is also evaluated during the numerical simulation and stored. Flow variables of all time steps are also stored, because these are used for the integration of the adjoint equation. Then the adjoint equation is integrated to obtain the gradient of $J(\boldsymbol{Q}_0)$. After obtaining the gradient, minimization of $J(\boldsymbol{Q}_0)$ was conducted by the quasi-Newton method through modifying the initial flow variable $\boldsymbol{Q}_0$. The Hessian matrix is approximated using the limited-memory Broyden–Fletcher–Goldfarb–Shanno (BFGS) method [22,23]. In this method, memory requirements are reduced because the approximated Hessian matrix is not stored explicitly. If the update of the initial flow variable is larger than a convergence threshold, the numerical simulation is performed using the updated initial flow vector and the preceding procedure is repeated again.

Evaluation of the difference between the flight data and numerical results was made at an arbitrary flight position in the computational domain, in which the flight data are interpolated in time to obtain flight data at an arbitrary time referred by the numerical simulation. Figure 3 shows the interpolation between the computational nodes and the flight position. To compare the flight data at the arbitrary flight position with the computational results, the results on the computational nodes surrounding the flight position are interpolated into the flight position. This procedure corresponds to the measurement operator H_i in Eq. (8). The $J(\boldsymbol{Q}_0)$ is evaluated from the difference between the flight data and the interpolated computational results. Then the difference is distributed from the flight position to the surrounding computational nodes to compute the forcing term of the adjoint equation in Eq. (18). These procedures are performed at every time step of the numerical simulation.

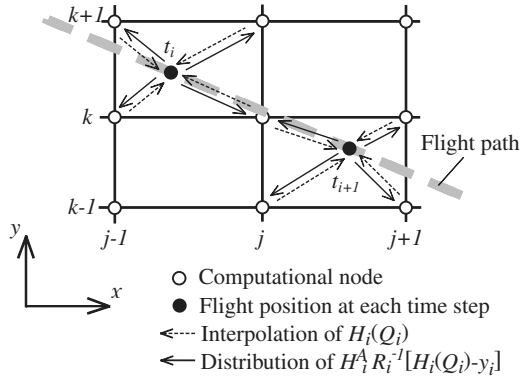

Fig. 3 Schematic of computations in measurement operator and adjoint forcing term.

III. Handling of Flight Data

The two encounters with severe turbulence, in which the change of vertical acceleration exceeds approximately one, are described. The wind velocity vector estimated from the flight data was integrated into the numerical simulation. The potential temperature was also incorporated into the numerical simulation. The time-dependent flight position and velocity vector at the position in the three-dimensional space were estimated as follows. The horizontal flight position was estimated by integrating a ground speed that is the output of the inertial navigation system. The vertical position was estimated from the pressure altitude. The horizontal velocity component was estimated from the true air speed, ground speed, heading of aircraft, and drift angle. The vertical velocity component was estimated from the true air speed, pitch angle, angle of attack, and climb rate of an aircraft [24]. Then the wind velocity vector was reduced to a two-dimensional vector consisting of flight distance direction and altitude direction components, because the numerical simulation was performed in two dimensions of these directions. The velocity vector and potential temperature at each flight position were used as measurement data. That is, only one velocity vector and potential temperature on the flight position were integrated into the numerical simulation at one time step. Vertical profiles of the horizontal velocity and potential temperature were used for the initial flow condition of the 4D-var method. These vertical profiles were obtained from the flight data or regional weather prediction results.

A. Case 1

This case was the turbulence that a Boeing 767 encountered at an altitude of approximately 4000 m during descent. Figure 4a shows the velocity components estimated from the flight data, and Fig. 4b shows the potential temperature and vertical acceleration. A drastic change of vertical velocity occurs from 2000 to 4000 m in distance. Maximum and minimum vertical acceleration were approximately 2.3 and 0.4, where the normal gravity condition corresponds to unity. Figure 4c shows vertical profiles of the horizontal wind and potential temperature. These were obtained from the flight data, in which a long range of the flight data was used to obtain the vertical profile. As shown in Fig. 4c, a large fluctuation of horizontal velocity, on the order of 1000 m in altitude direction, can be seen.

B. Case 2

In this case, an Airbus 320 encountered severe turbulence at an altitude of approximately 6500 m during ascent. Figure 5a shows the velocity components estimated from the flight data, and Fig. 5b shows the potential temperature and vertical acceleration. The peak of the vertical velocity component is not clear, compared with case 1; however, relatively large vertical velocity is seen in the range between 6000 and 9000 m in distance. The vertical profiles of the horizontal wind and potential temperature shown in Fig. 5c were given by a regional weather prediction model that has been used for planning a flight test in JAXA [25]. Initial and boundary conditions of the regional weather prediction model are given by a regional

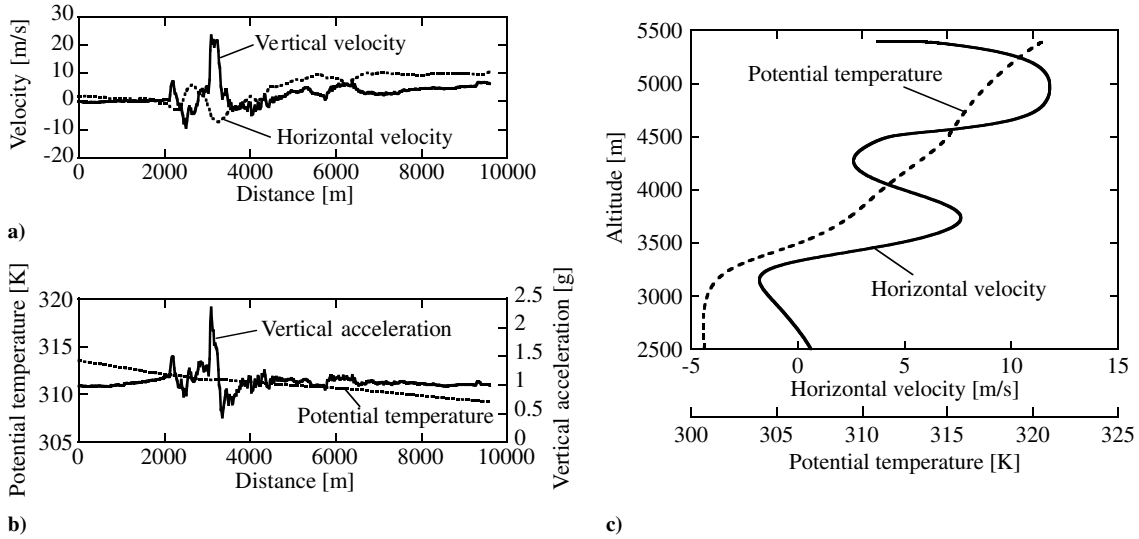

Fig. 4 Flight data for case 1: a) velocity components, b) vertical acceleration and potential temperature obtained from flight data, and c) vertical profiles of the horizontal velocity and potential temperature.

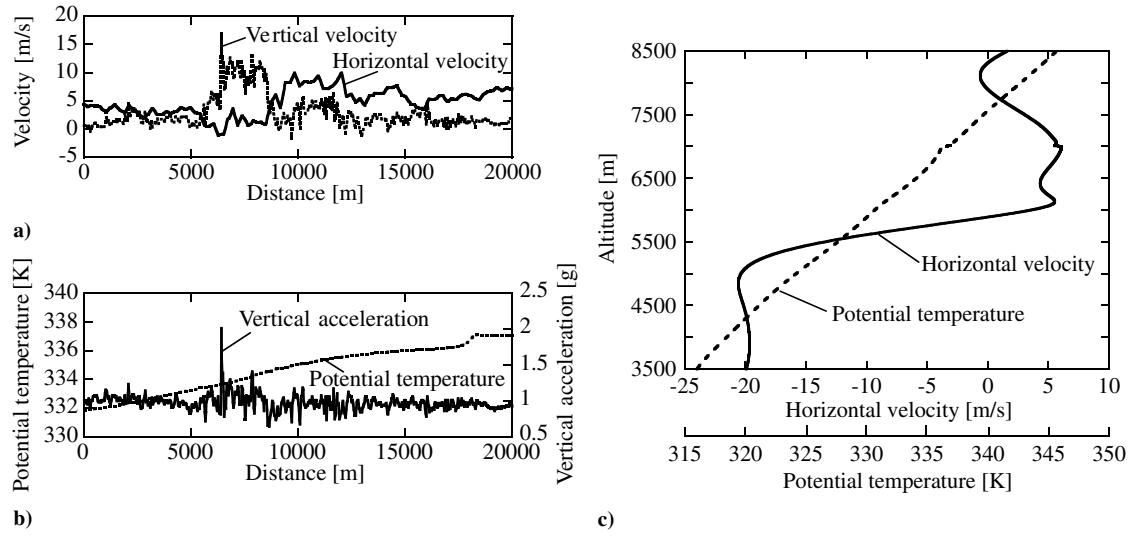

Fig. 5 Flight data for case 2: a) velocity components, b) vertical acceleration and potential temperature obtained from flight data, and c) vertical profiles of the horizontal velocity and potential temperature.

spectral model provided by the Japan Meteorological Agency. A jump in horizontal velocity indicates large vertical wind shear.

IV. Hazard Indices

The existing hazard indices F-factor and rms normal load were applied to the reproduced flowfield to evaluate their turbulence-prediction capability. Hazard indices calculated from the reproduced flowfield are used as a reference field for evaluation of the hazard indices obtained form radar or lidar simulation.

A. F-Factor

The F-factor in a two-dimensional vertical plane is represented as follows, with the assumption of a small flight path angle [3]:

$$F = \frac{V_g}{g}\frac{\partial u}{\partial x} - \frac{v}{V_a} \tag{20}$$

where V_g and V_a are ground speed and air speed, respectively. The relation $V_a = V_g - u$ is applied to obtain V_a, where constant flight speed and direction are assumed. F-factor represents the decrease of excess thrust due to wind shear, and positive value of the F-factor corresponds to a decline of virtual aircraft performance.

B. Root-Mean-Square Normal Load

The root-mean-square normal load $\sigma_{\Delta n}$ is based on a moving 5-s average of aircraft normal loads [10]. In this hazard index, $0.2\ \text{g} \leq \sigma_{\Delta n} < 0.3\ \text{g}$ corresponds to moderate turbulence and $\sigma_{\Delta n} \geq 0.3$ g means severe turbulence. It is shown that the peak of $\sigma_{\Delta n}$ is proportional to a peak normal load:

$$\Delta n|_{\text{peak}} = 2.6385\sigma_{\Delta n}|_{\text{peak}} + 0.0085789$$

The $\sigma_{\Delta n}|_{\text{peak}}$ is estimated from a moving 5-s average of vertical wind σ_w, assuming a specific aircraft. In the present study, the relationship between the $\sigma_{\Delta n}|_{\text{peak}}$ and the σ_w was obtained by formulas taken from Hamilton and Proctor [10]. The σ_w was computed from a reproduced flowfield based on the following equation:

$$\sigma_w(x) = \left[\frac{1}{L_x}\int_{x-\frac{L_x}{2}}^{x+\frac{L_x}{2}} \{v(x') - \bar{v}(x')\}^2\,\mathrm{d}x'\right]^{\frac{1}{2}} \tag{21}$$

where L_x is set to the flight distance of 5 s.

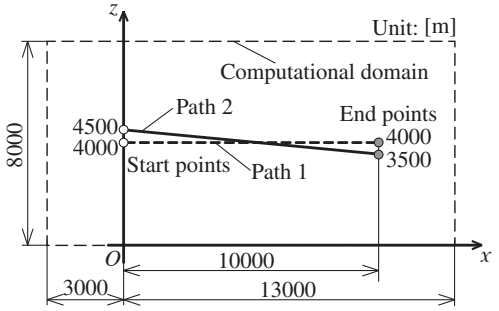

Fig. 6 Computational domain and setting of pseudo flight paths, path 1 and path 2. path 1 + 2 is a combination of path 1 and path 2 with 50 s of time lag.

V. Results

A. Numerical Experiment Using Pseudo Flight Data

A numerical experiment was performed to validate the method suggested here. In the numerical experiment, pseudo flight data were extracted from the target flowfield obtained from the numerical simulation of K–H instability and were used as measurements for the 4D-var method. The 4D-var method was applied to find the initial flowfield reproducing the target flowfield realized by the numerical simulation. Numerical uncertainties for computation of an atmospheric turbulence can be neglected by using the pseudo flight data obtained from the numerical simulation results; therefore, the capability of the 4D-var method coupled with spatially limited measurements was investigated here.

1. Computational Setup

The computational domain was two dimensions of 16,000 m in width and 8000 m in height, as shown in Fig. 6. The number of mesh points were 129 points for the width direction and 54 points for the height direction, respectively. The mesh spacing of the computational domain was approximately 120 m. Although a two-dimensional representation of the flowfield is not appropriate for turbulent flow simulation, a velocity component perpendicular to both flight path and altitude direction is not important, compared with the other two components in the actual flight condition. A target flowfield was set to the shear flow with disturbance, using a sine curve to initiate K–H instability. The velocity field of the target flow was determined by the following profiles:

$$u(x,y) = \begin{cases} 20 \text{ m/s} & (y \le 4000 \text{ m}) \\ -20 \text{ m/s} & (y > 4000 \text{ m}) \end{cases} \tag{22}$$

$$v(x,y) = 5 \sin \frac{10\pi x}{16,000} \exp\left\{-10\left(\frac{y-4000}{8000}\right)^2\right\} \text{ m/s} \tag{23}$$

where a wave number was chosen to enhance a development of vortices under the present flow conditions. The potential temperature was set to 300 K, and pressure was set to hydrostatic equilibrium. The computation was started from the preceding initial flow conditions, and a velocity vector on a pseudo flight position was extracted to create pseudo flight data at each time step. In this study, the pseudo flight path was assumed to be a straight line, and its start and end points were set to two cases named path 1 and path 2, as shown in Fig. 6. The flight time was set to 100 s for both cases. As a result, a ground speed V_g became approximately 100 m/s. In addition, a combination of path 1 and path 2, referred to as path 1 + 2, was considered to investigate the effect of the increased number of flight data points. Using the pseudo flight data extracted from the numerical simulation results, the 4D-var method was applied to the flowfield, starting from the shear flow without the initial disturbance for a vertical velocity component. Computational conditions, including a time-step size, were identical to those of the target flowfield. The computation was performed over 550 s, starting from −50 s, and the pseudo flight data were applied between 0 and 100 s, which corresponds to the period in which the pseudo flight data were extracted. In the case of path 1 + 2, path 1 was applied from −50 until 50 s, and path 2 was applied from 0 until 100 s. For all cases, only one velocity vector at the pseudo flight position was given as a measurement at each computational time step.

Figure 7 shows the target flowfield at several time steps. Initial disturbance is developed at $T = 0$ s, and "cat's-eye" vortices are seen at $T = 50$ s. A relatively stable flow state continued until $T = 200$ s. On the other hand, the shear flow without the initial disturbance did not show any development of vortices in the present conditions. It is speculated from these results that the initial disturbance played an important role in the time development of the shear flow. Because the K–H instability is a highly unsteady flow phenomenon, the resulting flowfield starting from different initial conditions results in a significantly different unsteady flow state.

Pseudo flight data extracted from the target flowfield for path 1 and path 2 are shown in Figs. 8 and 9. In these figures, the solid line corresponds to the vertical velocity component and the dotted line shows the horizontal velocity component. Velocity components have asymmetric distribution in the horizontal direction, despite the target flowfield being symmetric, because the pseudo flight data were extracted on each flight position at different times from an unsteady flowfield. Fluctuations of velocity components are due to cat's-eye vortices of K–H instability. For the case of path 2, a horizontal velocity increases from −28 to 28 m/s, with involved fluctuations due to the cat's-eye vortices, because path 2 is slightly slanted off the horizontal.

2. Dependence of the Reproduced Flowfield on the Pseudo Flight Path

The 4D-var method was applied to the pseudo flight data extracted from the target flowfield shown in Fig. 7. Figure 10 shows the

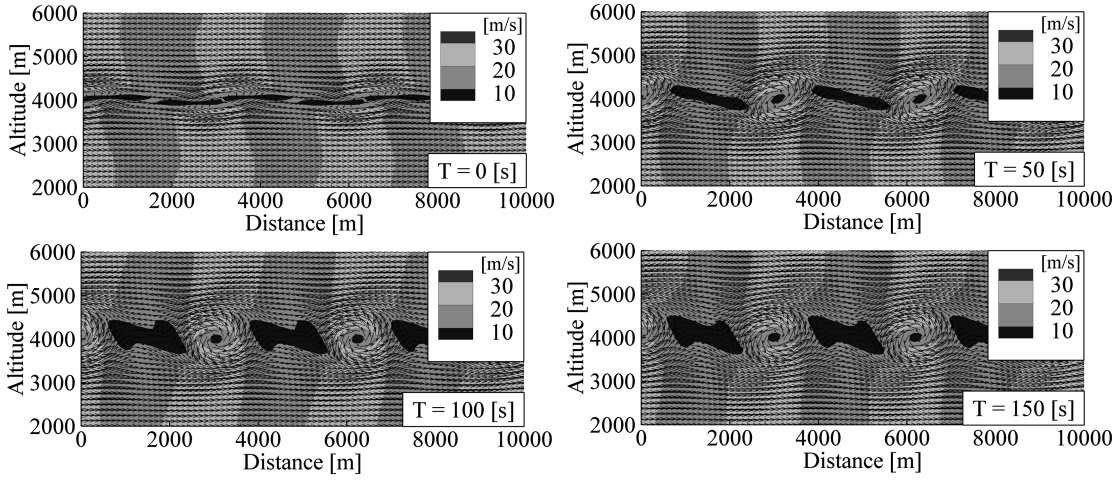

Fig. 7 K–H instability flow used for the target flowfield.

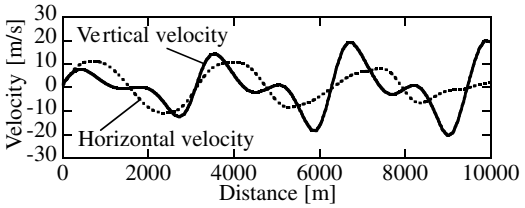

Fig. 8 Pseudo flight data for path 1.

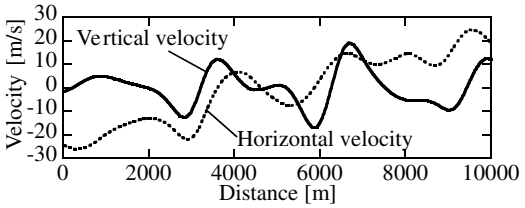

Fig. 9 Pseudo flight data for path 2.

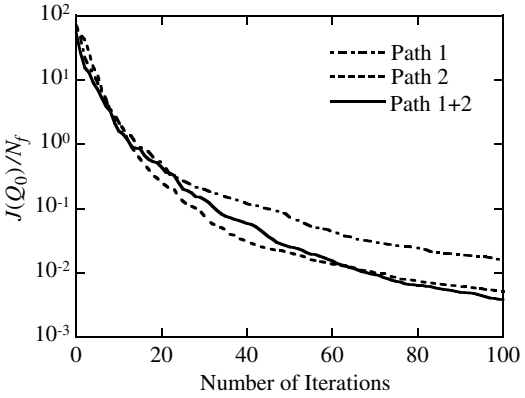

Fig. 10 Minimization history of objective function per number of data along the flight path.

minimization histories of objective function $J(\boldsymbol{Q}_0)$ for path 1, path 2, and path $1+2$. Here, $J(\boldsymbol{Q}_0)$ is divided by the number of data along the pseudo flight path, because the number of data used to evaluate $J(\boldsymbol{Q}_0)$ varies depending on the pseudo flight paths. During the 4D-var method iterations, the velocity vector and potential temperature at flight position were assimilated. For all cases, the $J(\boldsymbol{Q}_0)/N_f$ decreases on the order of 10^3 after 100 iterations of the 4D-var method. The reason for the large $J(\boldsymbol{Q}_0)/N_f$ of path 1 compared with path 2 at the 100th iteration is because path 1 involves large fluctuations of velocity, because the pseudo flight path passes through the center of the vortex street. On the other hand, path 2 is slightly displaced from the center of the vortex street; therefore, the fluctuations of velocity on path 2 are smaller than those of path 1, and this leads to the smaller $J(\boldsymbol{Q}_0)/N_f$ than for path 1. For path $1+2$, $J(\boldsymbol{Q}_0)/N_f$ became smaller than that of path 1 and path 2. This implies that the difference between the pseudo flight data and corresponding flow variables of the reproduced flowfield decreases as the number of sampling points increases. The minimization histories of $J(\boldsymbol{Q}_0)/N_f$ reveal that the present 4D-var method works even when only one velocity vector is given as measurement data at one time step.

The reproduced flowfields for path 1 and path 2 are shown in Figs. 11 and 12, respectively. In these figures, the velocity vector and contour of velocity magnitude are also shown. Although the reproduced flowfield involves small fluctuations of velocity distribution compared with the target flowfield, a vortex street that consists of four vortices is reproduced for both cases, as shown in these figures. For path 2, the flowfield is more disturbed compared with that of path 1, especially, at $T = 0$ and 50 s. Vortices in the left side of the computational domain appear weaker than those of path 1. The reason for these weak vortices is because the early part of the pseudo flight data of path 2, which is used as a measurement on the left-side region, does not include the information of the vortex street, because of the higher flight position. Figure 13 shows the reproduced flowfields for path $1+2$. The reproduced flowfield is similar to that of path 1; however, a flowfield at $T = 0$ s is much closer to the target flowfield than with path 1. It is confirmed that an increased number of pseudo flight data improves flowfield reproducibility.

Figures 14 and 15 show the histories of the minimum and maximum differences of the velocity magnitude between the target and reproduced flowfield along the flight path for path 1 and path 2, respectively. The decreases of the minimum and maximum differences saturate at around the 50th iteration, although $J(\boldsymbol{Q}_0)/N_f$ keeps decreasing, as shown in Fig. 10. This implies that the decrease of $J(\boldsymbol{Q}_0)/N_f$ after the 50th iteration is mainly due to the agreement of the time evolution of the flowfield with that of the target. The maximum difference of the velocity magnitude was on the order of 0.1 m/s for both cases. Figure 16 shows the result for the case of path $1+2$. A tendency similar to path 1 and path 2 is observed; however, the decrease rate of the maximum difference around 80 to 100 iterations is larger than with path 1 and path 2.

Although it is difficult to identify a high degree of freedom of Navier–Stokes equations by a limited number of measurements, reasonable reproducibility was obtained by using the present method. And better reproducibility of the flowfield is expected when the measurements include the primary features of the target flowfield.

B. Numerical Simulation of CAT by Integrating Flight Data

Reproducibility of the flowfield using the 4D-var method with limited measurements, one velocity vector per each time step, was

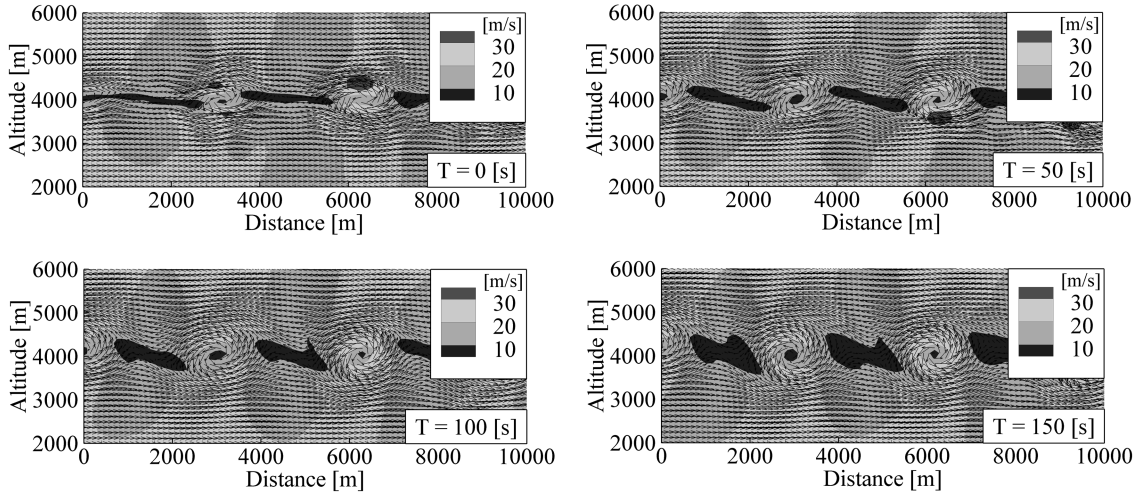

Fig. 11 Reproduced flowfields for path 1.

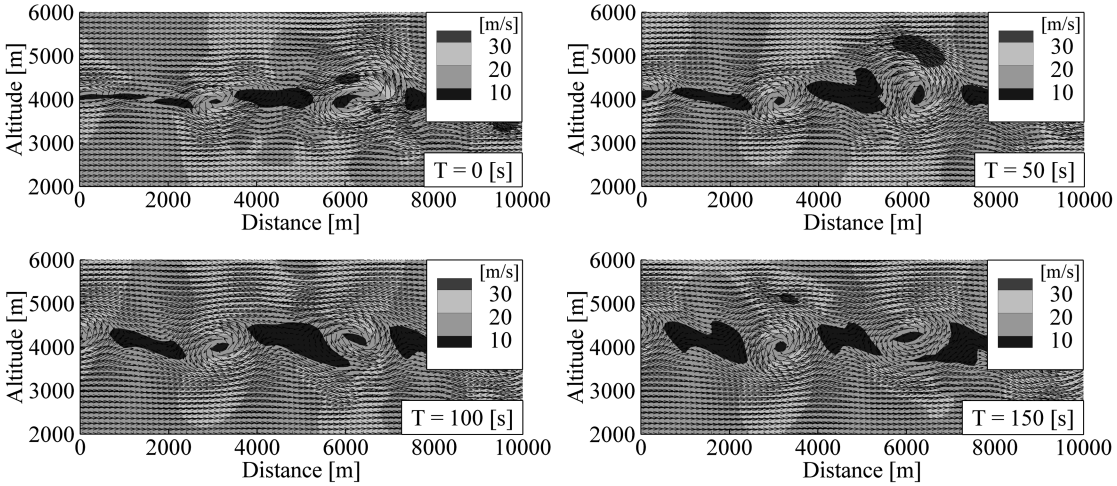

Fig. 12 Reproduced flowfields for path 2.

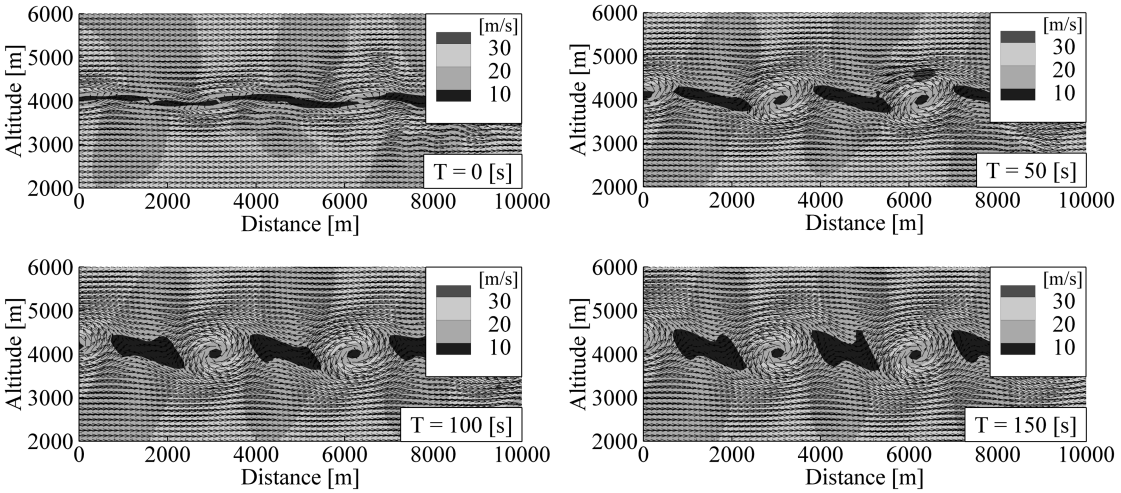

Fig. 13 Reproduced flowfields for path 1 + 2.

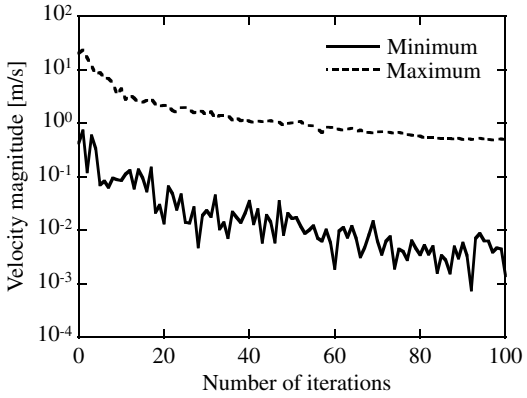

Fig. 14 Minimum and maximum differences of velocity magnitude along the flight path for path 1.

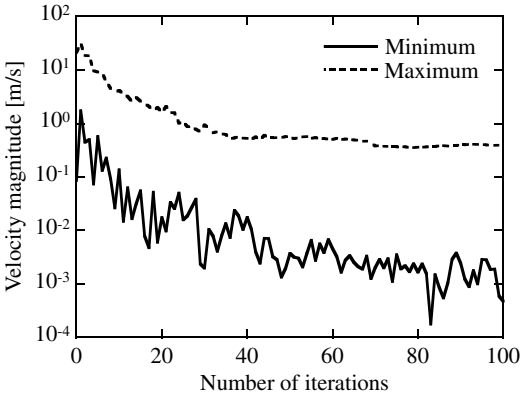

Fig. 15 Minimum and maximum differences of velocity magnitude along the flight path for path 2.

confirmed by numerical experiments in the previous section. Here, the numerical simulation was performed by integrating two cases of actual flight data.

1. *Computational Setup*

The computational domain for case 1 was 16,000 m in the horizontal direction and 8000 m in the vertical direction, and that for case 2 was 26,000 m in the horizontal direction and 14,000 m in the vertical direction. The horizontal axis corresponds to the flight distance, and the vertical axis corresponds to the altitude. Two different mesh densities were examined for both cases. The numbers of mesh points were 150×64 (coarse) and 200×86 (fine) for case 1. And the numbers of mesh points were 250×120 (coarse) and 375×180 (fine) for case 2. The mesh spacing in the center of the computational domain was approximately 100 m for coarse and 75 m for fine meshes.

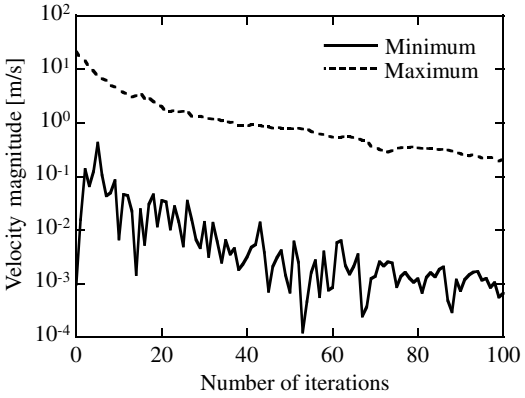

Fig. 16 Minimum and maximum differences of velocity magnitude along the flight path for path 1 + 2.

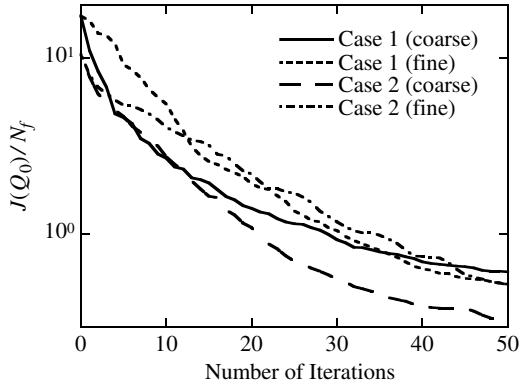

Fig. 17 Minimization histories of objective function for actual flight data.

2. Reproduction of CAT

Figure 17 shows the histories of the objective function $J(\boldsymbol{Q}_0)/N_f$ for case 1 (coarse), case 1 (fine), case 2 (coarse), and case 2 (fine). The objective function decreases on the order of 10^2 after 50 iterations of the 4D-var method for all cases. The decreases of the $J(\boldsymbol{Q}_0)/N_f$ appear in similar magnitudes for all cases, although different flight data and computational mesh points were employed. However, it is apparent that finer-mesh computation degrades the convergence property from the comparison of coarse- and fine-mesh cases. Because the root-mean-square sum of the difference between the measurements and computation is used to obtain the $J(\boldsymbol{Q}_0)/N_f$, the $J(\boldsymbol{Q}_0)/N_f$ simply increases as the number of mesh points increases. It is also considered that the increase of the degree of freedom to be determined by the measurements with increasing mesh points affects the convergence property.

Figure 18 shows the flowfields at the 50th iteration of the 4D-var method for case 1 (fine). The velocity vector and contour of velocity magnitude are shown in these figures. The flowfield at $T = 20$ s in Fig. 18 corresponds to the time when an aircraft encountered CAT. Sudden changes of the vertical wind of the flight data result in vortices in this region. The primary vortices are pair vortices that have opposite rotational directions, and a strong upwind is created between these pair vortices. Figure 19 shows the results for case 2 (fine). In this case, $T = 30$ s corresponds to the time when an aircraft encountered turbulence. An increase of upward wind is seen at $T = 30$ and 70 s, and the upward wind spreads along the horizontal direction. A clear vortex structure cannot be seen in this case.

From the comparison of the results between coarse and fine meshes, the mesh density only affects the duration time of the vortices, not the strength of the vortices for case 1 and the strength of the upward wind for case 2. However, the two-dimensional computation employed in this study is not accurate enough to evaluate the decay time of the vortices. The results using the coarse mesh show a reasonable vortex structure of CAT in comparison with the fine-mesh case. Therefore, the information about the local wind strength of CAT can be predicted even on a coarse mesh.

Figures 20 and 21 show the minimum and maximum differences of the velocity magnitude along the flight path for case 1 (fine) and case 2 (fine), respectively. As shown in these figures, decreases of the minimum and maximum differences are slow compared with the convergence history of $J(\boldsymbol{Q}_0)/N_f$. This tendency is similar to the previous numerical experiments. In the case of actual flight data, the initial flowfield of the 4D-var method was given so that they became as similar to real flowfield as possible, based on the vertical profiles of the horizontal velocity and the potential temperature obtained from

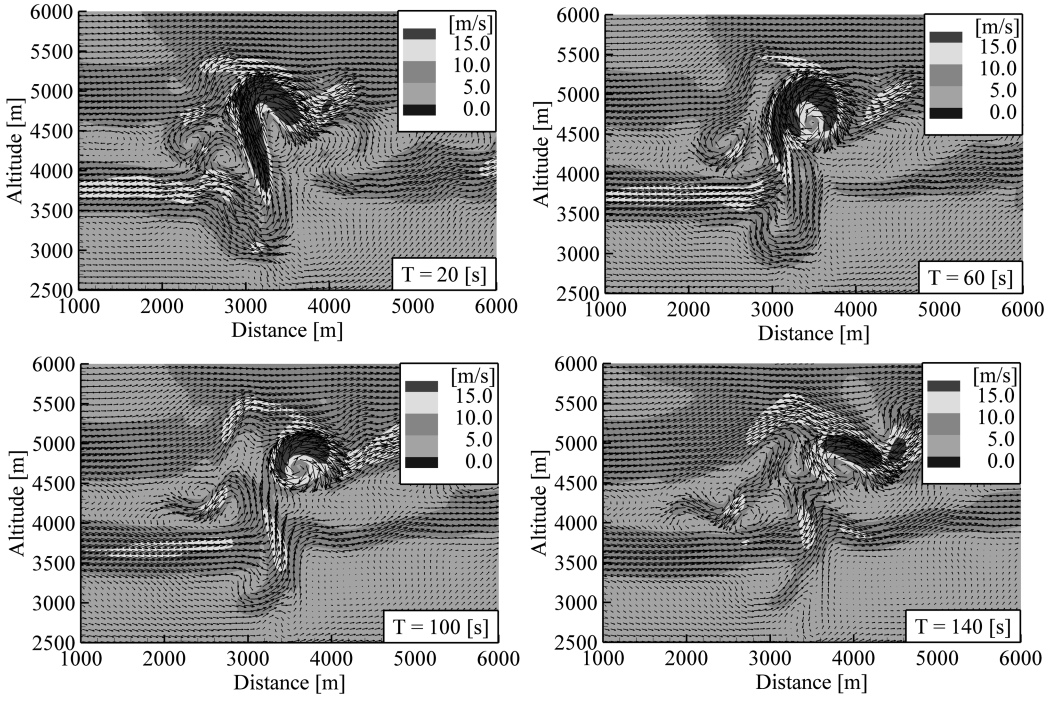

Fig. 18 Reproduced flowfields at $T = 20, 60, 100$, and 140 s for case 1 (fine), where $T = 20$ s corresponds to maximum vertical acceleration in flight data.

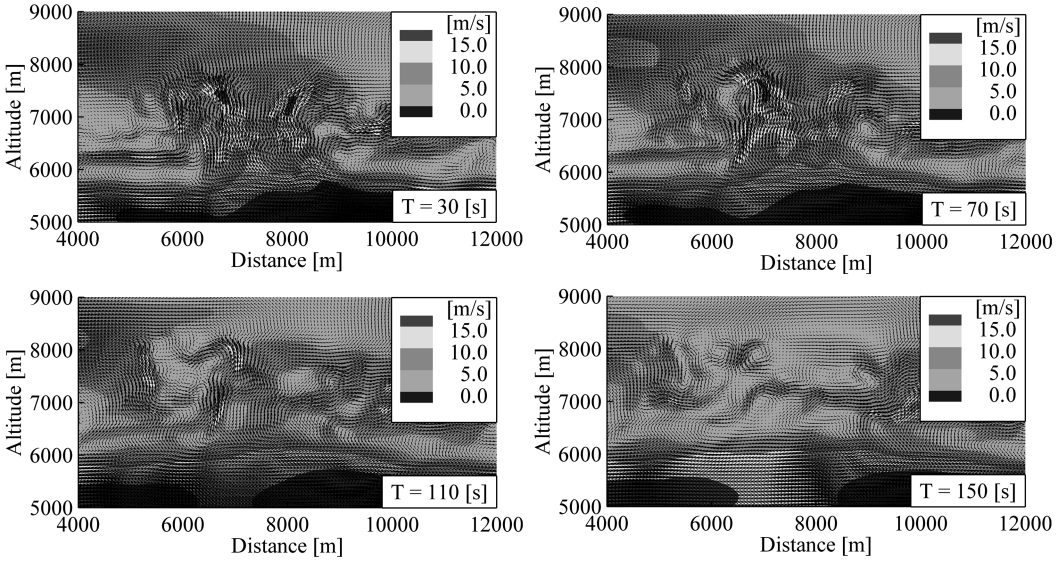

Fig. 19 Reproduced flowfields at $T = 30, 70, 110$, and 150 s for case 2 (fine), where $T = 30$ s corresponds to maximum vertical acceleration in flight data.

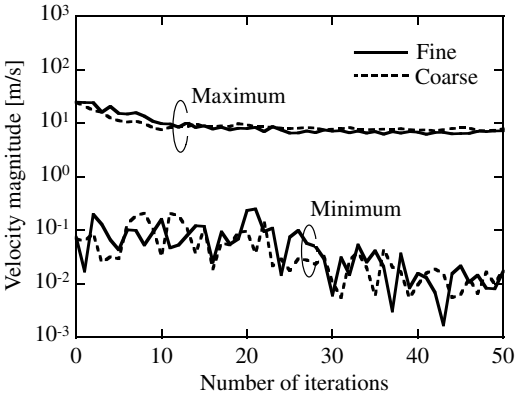

Fig. 20 Minimum and maximum differences of velocity magnitude along the flight path for case 1 (fine).

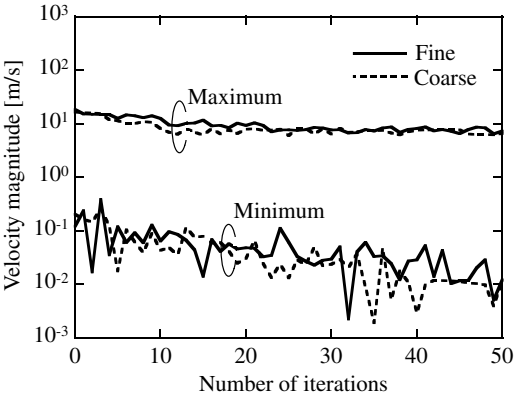

Fig. 21 Minimum and maximum differences of velocity magnitude along the flight path for case 2 (fine).

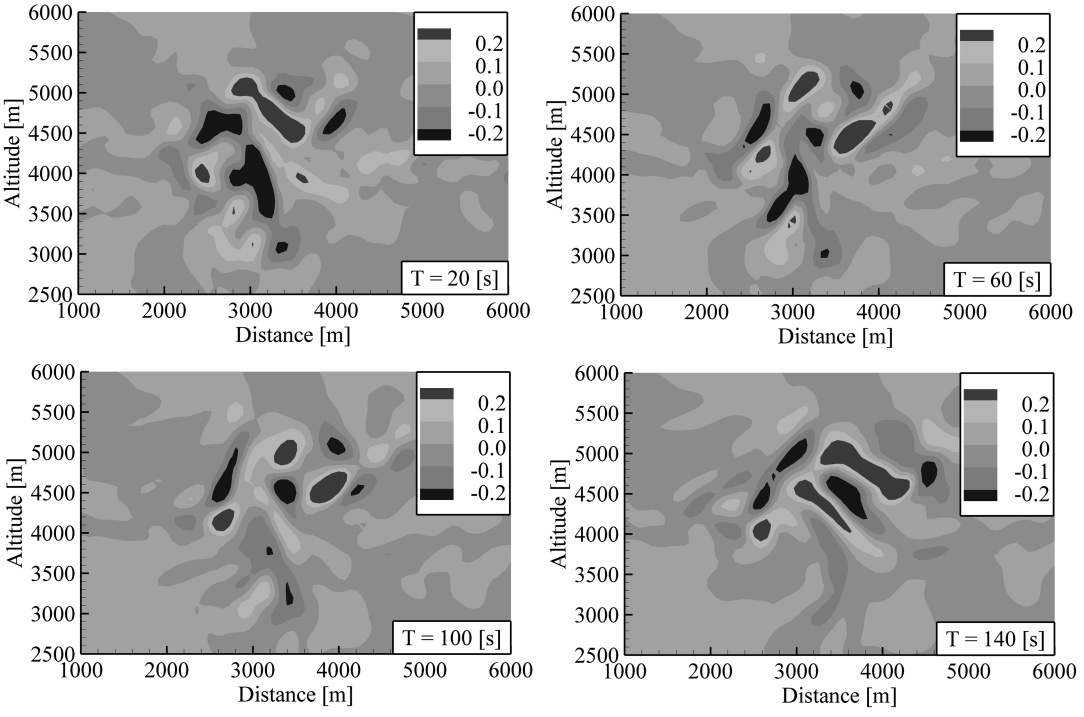

Fig. 22 Distributions of the F-factor for case 1 (fine), in which time stamps correspond to Fig. 18.

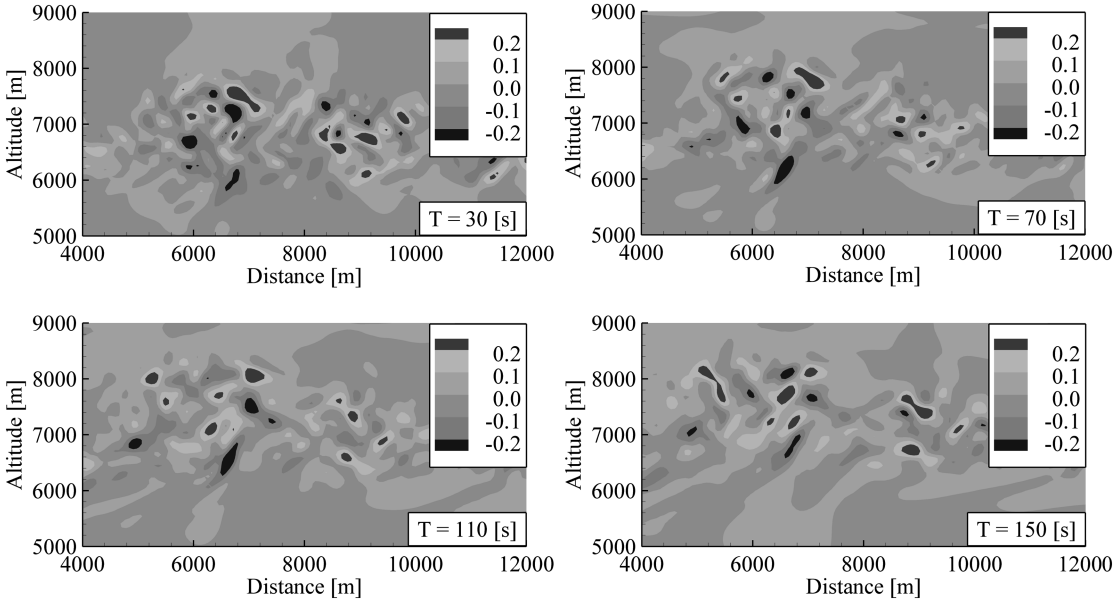

Fig. 23 Distributions of the *F*-factor for case 2 (fine), in which time stamps correspond to Fig. 19.

flight data or weather prediction results, for faster convergence. As a result, the decrease of the maximum velocity magnitude was not so significant. The maximum differences of the velocity magnitude between the flight data and numerical results are the order of 1 m/s for all cases that use actual flight data.

C. Hazard Analysis

Figures 22 and 23 show the distributions of the *F*-factor for case 1 (fine) and case 2 (fine), respectively. A large *F*-factor is seen in the region in which large vertical acceleration was observed in the flight data for both case 1 and case 2. The region also corresponds to that in which strong upwind was reproduced. A spotted distribution of the *F*-factor for case 2 is finer than that for case 1. Because the *F*-factor is calculated from the derivative of wind velocity, the distribution is significantly affected by the fluctuation of wind velocity, especially by the vertical wind component.

Figures 24 and 25 show the distributions of the a peak normal load estimated from the root-mean-square normal load $\sigma_{\Delta n}$, assuming a specific aircraft [10]. In these figures, the contour map is plotted by the deviation from the standard gravity condition in the unit of gravity; that is, 1 *g* corresponds to the standard gravity condition. The region of large peak normal load agrees with that of the large *F*-factor. The peak normal load has a smooth distribution compared with that of the *F*-factor and covers the region in which the strong vortices exist. For case 2 (fine), a strong upwind region is clearly captured by the peak normal load, compared with the *F*-factor shown in Fig. 23.

For use of the obtained hazard field as a reference hazard field for lidar or radar simulation, smooth distribution obtained from the peak

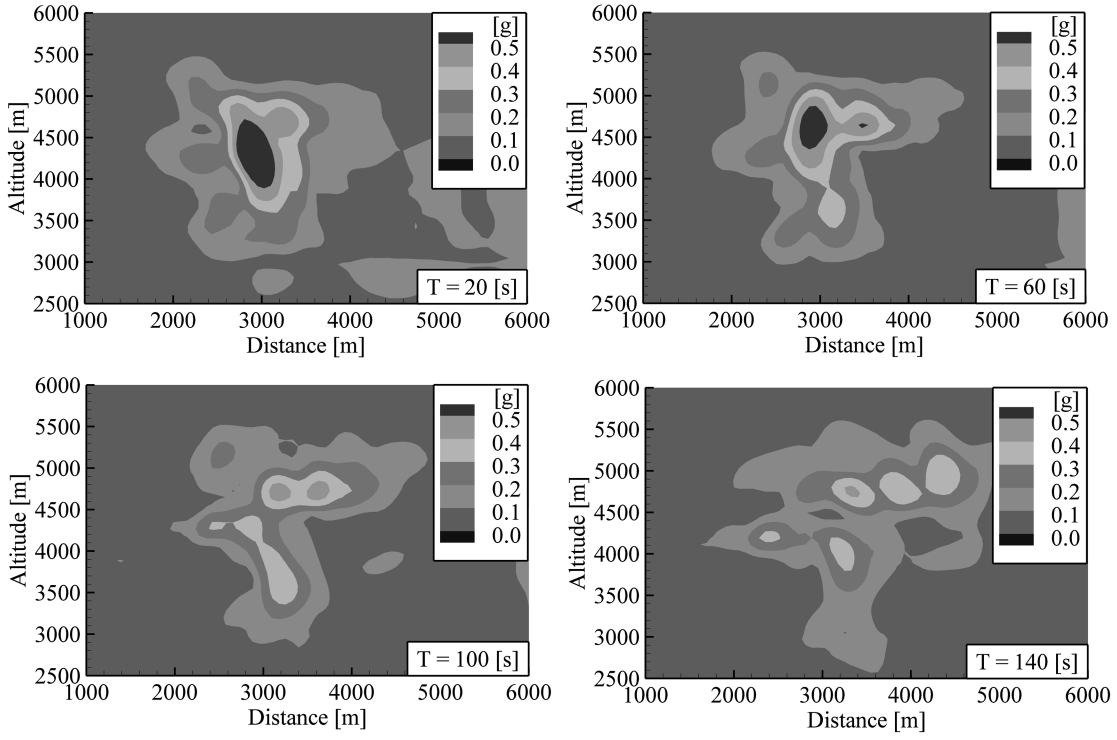

Fig. 24 Distributions of the peak normal load for case 1 (fine), in which time stamps correspond to Fig. 18.

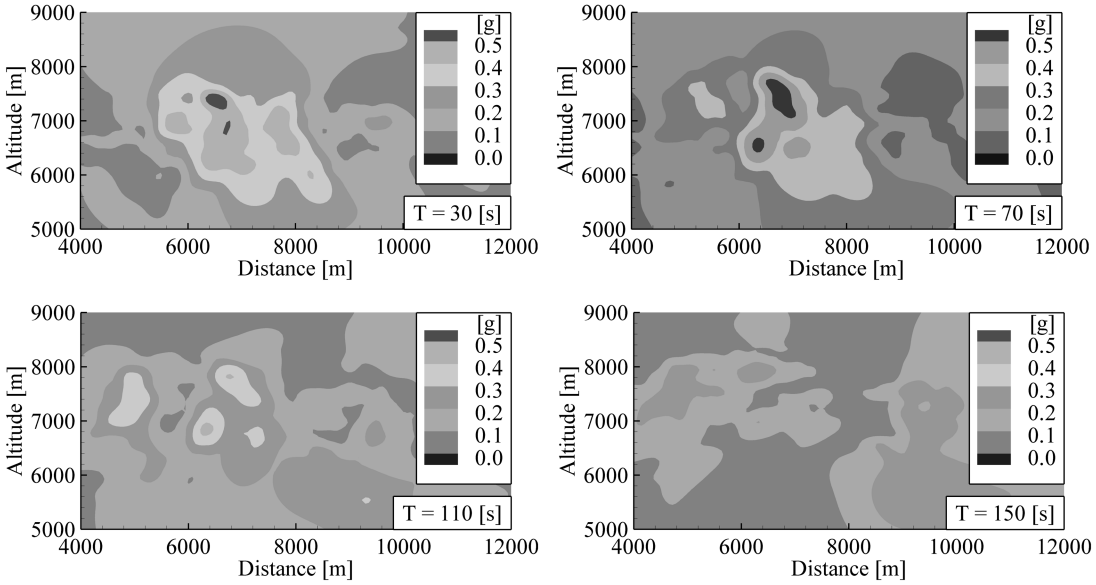

Fig. 25 Distributions of the peak normal load for case 2 (fine), in which time stamps correspond to Fig. 19.

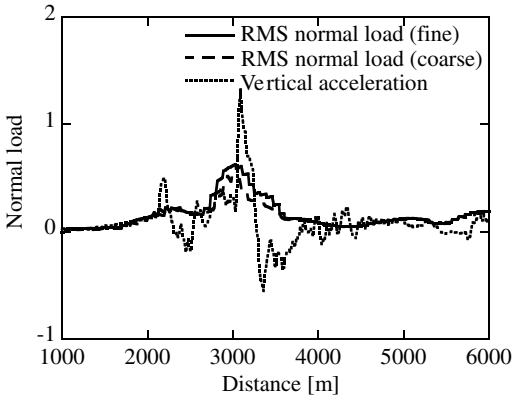

Fig. 26 Comparisons of peak normal load and vertical acceleration obtained from flight data along the flight path for case 1.

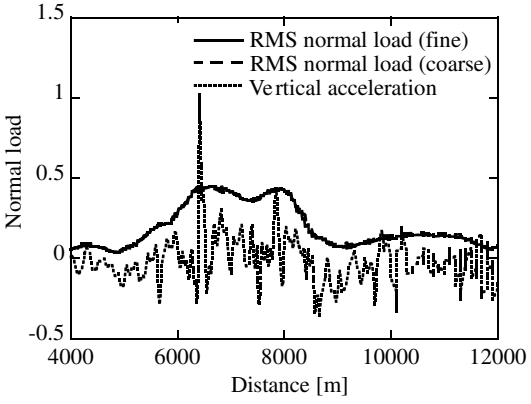

Fig. 27 Comparisons of peak normal load and vertical acceleration obtained from flight data along the flight path for case 2.

normal load would be appropriate if the resolution was assumed to be several hundred meters. Otherwise, a hazard field with finer hazard distribution is obtained from the F-factor. The difference of mesh density did not indicate a large influence on the distribution of the evaluated hazard indices for both case 1 and case 2.

Figures 26 and 27 show the comparisons of the estimated peak normal load along the flight path and vertical acceleration obtained from the flight data for case 1 and case 2, respectively. Both peak normal load and gravity acceleration are shown by the deviation from the standard gravity condition in the unit of gravity. From these results, the peak normal load represents the tendency of the vertical acceleration, although its peaks could not be captured, because the root-mean-square normal load was evaluated at 5-s intervals of flight time. The dependence on mesh density is seen near the large peak of vertical acceleration in the flight data for case 1. On the other hand, the mesh dependency is not seen in case 2, because the fluctuations of wind velocity obtained from coarse and fine-mesh computations are fine enough to evaluate the 5-s intervals of peak normal load.

VI. Conclusions

In this study, the numerical simulation of clear air turbulence was carried out by integrating flight data based on the 4D-var method. Objective function of the 4D-var method, which is determined by the difference between the flight data and the numerical simulation results, was successfully minimized using the gradient obtained from an adjoint code and the quasi-Newton method. The validation of the 4D-var method was made by using pseudo flight data extracted from reference numerical simulation results. The results showed the reproducibility of a flowfield by using spatially limited measurements: for example, flight data. The reproduced flowfield is affected by whether the pseudo flight data include dominant flow features. Then the 4D-var method was applied to two cases of actual flight data. Resulting flowfields showed a flowfield dominated by a vortex pair and a flowfield dominated by a broad upwind region, depending on the applied flight data. Hazard indices were evaluated from the reproduced turbulence flowfield, and good correlations between the evaluated hazard and vertical acceleration of actual flight data were obtained.

Acknowledgment

The authors would like to thank the Advanced Fluid Information Research Center in the Institute of Fluid Science, Tohoku University, for the computational resources used in the present research.

References

[1] Asaka, K., Fujiwara, T., Inagaki, T., Harigae, M., Kameyama, S., Ando, T., and Hirano, Y., "Airborne Coherent Doppler Lidar—Flight Test Results," *Proceedings of the 43rd Aircraft Symposium* [CD-ROM], The Japan Society for Aeronautical and Space Science, Tokyo, Oct. 2005, Paper 3C9 (in Japanese).

[2] Endo, E., Harigae, M., and Asaka, K., "Method for Detection of Turbulence Using Variation of Head Wind," *Proceedings of the 44th Aircraft Symposium* [CD-ROM], The Japan Society for Aeronautical and Space Science, Tokyo, Oct. 2006, Paper 1D8 (in Japanese).

[3] Oseguera, R. M., and Bowles, R. L., "Airborne In Situ Computation of the Wind Shear Hazard Index," AIAA Paper 92-0291, 1992.
[4] Stewart, E. C., "Description of a Normal-Force In-Situ Turbulence Algorithm for Airplanes," NASA TM-2003-212666, 2003.
[5] Cornman, L., Morse, C., and Cunning, G., "Real-Time Estimation of Atmospheric Turbulence Severity from In-Situ Aircraft Measurement," AIAA Paper 94-0268, 1994.
[6] Hinton, D. A., "Forward-Look Wind-Shear Detection for Microburst Recovery," *Journal of Aircraft*, Vol. 29, No. 1, 1992, pp. 63–66.
[7] Stratton, D. A., and Stengel, R. F., "Robust Kalman Filter Design for Predictive Wind Shear Detection," *IEEE Transactions on Aerospace and Electronic Systems*, Vol. 29, No. 4, 1993, pp. 1185–1194. doi:10.1109/7.259521
[8] Mehta, R. S., "Modeling Clear-Air Turbulence with Vortices Using Parameter-Identification Techniques," *Journal of Guidance, Control, and Dynamics*, Vol. 10, No. 1, 1987, pp. 27–31.
[9] Parks, E. K., Wingrove, R. C., Bach, R. E., and Mehta, R. S., "Identification of Vortex-Induced Clear Air Turbulence Using Airline Flight Records," *Journal of Aircraft*, Vol. 22, No. 2, 1985, pp. 124–129.
[10] Hamilton, D. W., and Proctor, F. H., "An Aircraft Encounter with Turbulence in the Vicinity of a Thunderstorm," AIAA Paper 2003-4075, 2003.
[11] Hamilton, D. W., and Proctor, F. H., "Airborne Turbulence Detection System Certification Tool Set," AIAA Paper 2006-0075, 2006.
[12] Proctor, F. H., Hamilton, D. W., and Bowles, R. L., "Numerical Study of a Convective Turbulence Encounter," AIAA Paper 2002-0944, 2002.
[13] Proctor, F. H., "The NASA-Langley Wake Vortex Modeling Effort in Support of an Operational Aircraft Spacing System," AIAA Paper 98-0589, 1998.
[14] Proctor, F. H., and Han, J., "Numerical Study of Wake Vortex Interaction with the Ground Using the Terminal Area Simulation System," AIAA Paper 99-0754, 1999.
[15] Proctor, F. H., Hamilton, D. W., and Han, J., "Wake Vortex Transport and Decay in Ground Effect: Vortex Linking with the Ground," AIAA Paper 2000-0757, 2000.
[16] Switer, G. F., and Proctor, F. H., "Numerical Study of Wake Vortex Behavior in Turbulent Domains with Ambient Stratification," AIAA Paper 2000-0755, 2000.
[17] Tsuyuki, T., "Variational Data Assimilation in the Tropics Using Precipitation Data," *Meteorology and Atmospheric Physics*, Vol. 60, Nos. 1/3, 1996, pp. 87–104. doi:10.1007/BF01029787
[18] Evensen, G., "The Ensemble Kalman Filter: Theoretical Formulation and Practical Implementation," *Ocean Dynamics*, Vol. 53, No. 4, 2003, pp. 343–367. doi:10.1007/s10236-003-0036-9
[19] Funamoto, K., Hayase, T., Saijo, Y., and Yambe, T., "Fundamental Study of Transient Characteristics of Ultrasonic-Measurement-Integrated Simulation Toward Reproduction of Unsteady Blood Flows," *Proceedings of the ASME 2006 Summer Bioengineering Conference* [CD-ROM], American Society of Mechanical Engineers, New York, June 2006, Paper 4-11.
[20] Kalnay, E., *Atmospheric Modeling, Data Assimilation and Predictability*, Cambridge Univ. Press, Cambridge, England, U.K., 2003, Chap. 5.
[21] Yamamoto, S., and Daiguji, H., "Higher-Order-Accurate Upwind Schemes for Solving the Compressible Euler and Navier–Stokes Equations," *Computers and Fluids*, Vol. 22, Nos. 2–3, 1993, pp. 259–270. doi:10.1016/0045-7930(93)90058-H
[22] Averick, B. M., and More, J. J., "Evaluation of Large-Scale Optimization Problems on Vector and Parallel Architectures," *SIAM Journal on Optimization*, Vol. 4, No. 4, 1994, pp. 708–721. doi:10.1137/0804041
[23] Veerse, F., Auroux, D., and Fisher, M., "Limited-Memory BFGS Diagonal Preconditioners for a Data Assimilation Problem in Meteorology," *Optimization and Engineering*, Vol. 1, No. 3, 2000, pp. 323–339. doi:10.1023/A:1010030224033
[24] Stewart, E. C., "A Study of Airline Passenger Susceptibility to Atmospheric Turbulence Hazards," AIAA Paper 2000-3978, 2000.
[25] Oikawa, H., Inokuchi, H., and Igarashi, K., "Observation and Prediction System of Turbulence," *Proceedings of the 44th Aircraft Symposium* [CD-ROM], The Japan Society for Aeronautical and Space Science, Tokyo, Oct. 2006, Paper 3C11 (in Japanese).